Epitaxial integration and properties of $SrRuO_3$ on silicon

Cite as: APL Mater. **6**, 086101 (2018); https://doi.org/10.1063/1.5041940
Submitted: 28 May 2018 • Accepted: 08 July 2018 • Published Online: 02 August 2018

Zhe Wang, Hari P. Nair, Gabriela C. Correa, et al.

APL Mater. **6**, 086101 (2018); https://doi.org/10.1063/1.5041940

APL MATERIALS **6**, 086101 (2018)

Epitaxial integration and properties of $SrRuO_3$ on silicon

Zhe Wang,[1,a] Hari P. Nair,[2,a] Gabriela C. Correa,[2] Jaewoo Jeong,[3]
Kiyoung Lee,[4] Eun Sun Kim,[5] Ariel Seidner H.,[2] Chang Seung Lee,[4]
Han Jin Lim,[5] David A. Muller,[1,6] and Darrell G. Schlom[2,6,b]
[1]*School of Applied and Engineering Physics, Cornell University, Ithaca, New York 14853, USA*
[2]*Department of Materials Science and Engineering, Cornell University, Ithaca, New York 14853, USA*
[3]*New Memory Technology Lab, Semiconductor R&D Center, Samsung Electronics, Milpitas, California 95053, USA*
[4]*Platform Technology Laboratory, Samsung Advanced Institute of Technology (SAIT), Samsung Electronics, 130 Samsung-ro, Yeongtong-gu, Suwon-si, Gyeonggi-do 16678, South Korea*
[5]*Samsung Semiconductor R&D Center 1, Samsungjeonja-ro, Hwaseong-si, Gyeonggi-do 18448, South Korea*
[6]*Kavli Institute at Cornell for Nanoscale Science, Ithaca, New York 14853, USA*

(Received 28 May 2018; accepted 8 July 2018; published online 2 August 2018)

We report the integration of $SrRuO_3$, one of the most widely used oxide electrode materials in functional oxide heterostructures, with silicon using molecular-beam epitaxy and an $SrTiO_3$ buffer layer. The resulting $SrRuO_3$ film has a rocking curve full width at half maximum of 0.01°, a resistivity at room temperature of 250 $\mu\Omega$ cm, a residual resistivity ratio ($\rho_{300\ \mathrm{K}}/\rho_{4\ \mathrm{K}}$) of 11, and a paramagnetic-to-ferromagnetic transition temperature of ~160 K. These structural, electrical, and magnetic properties compare favorably to the best reported values for $SrRuO_3$ films on silicon and rival those of epitaxial $SrRuO_3$ films produced directly on $SrTiO_3$ single crystals by thin film growth techniques other than molecular-beam epitaxy. These high quality $SrRuO_3$ films with metallic conductivity on silicon are relevant to integrating multi-functional oxides with the workhorse of semiconductor technology, silicon.
https://doi.org/10.1063/1.5041940

$SrRuO_3$ is one of the most widely used oxide electrode materials in epitaxial oxide heterostructures and related devices.[1] This utility arises from its excellent thermochemical stability,[2,3] high conductivity at room temperature, and especially because of its close lattice match ($SrRuO_3$ has a pseudocubic lattice parameter of 3.93 Å) with many functional perovskite oxides. These include multiferroics such as $BiFeO_3$ (pseudocubic lattice parameter of 3.96 Å),[4] ferroelectrics such as $BaTiO_3$ (in-plane lattice parameter of 3.99 Å),[5] superconductors such as $YBa_2Cu_3O_{7-x}$ (in-plane pseudotetragonal lattice parameter of 3.85 Å),[6] and piezoelectrics such as $Pb(Zr,Ti)O_3$ (in-plane lattice parameter 3.905–4.14 Å).[7,8] $SrRuO_3$ is often employed in ferroelectric devices,[9] superconducting multilayers,[10] Josephson junctions,[11] electro-optic and magneto-optic devices,[12] Schottky junctions,[13] ferroelectric tunnel junctions,[14] magnetocaloric devices,[15] resistivity switching devices,[14,16] magnetoelectric devices,[17,18] photovoltaic devices,[19] and optoelectronic devices.[20] In condensed matter physics, $SrRuO_3$ also plays an active role in moderately correlated materials physics due to its unusual itinerant ferromagnetism as a 4*d* transition metal oxide. The transport properties of $SrRuO_3$ also draw great attention, including its Fermi liquid behavior at low temperature[21] and bad metallic behavior at high temperature.[22] Recently, heterostructures involving $SrRuO_3$ layers have been shown to exhibit the topological Hall effect[23] and the inverse spin Hall effect,[24] indicating its potential for spintronic applications.

---

[a] Zhe Wang and Hari P. Nair contributed equally to this work.

[b] Author to whom correspondence should be addressed: schlom@cornell.edu.

Integration of $SrRuO_3$ with silicon, the backbone of the electronics industry, is critical for leveraging the extensive existing infrastructure for large-scale semiconductor manufacturing. This will enable the widespread use of $SrRuO_3$-based multi-functional oxide heterostructures for a wide range of applications.

Unfortunately, directly integrating epitaxial $SrRuO_3$ on silicon is difficult as the formation of an amorphous SiO_2 layer in the oxidative environment during the growth of $SrRuO_3$ can impede epitaxial growth, resulting in polycrystalline $SrRuO_3$ films.[25] Polycrystalline $SrRuO_3$ precludes the epitaxial integration of functional oxide thin films on top of the $SrRuO_3$ electrode and with it a loss of the optimal properties that epitaxial heterostructures often provide for complex oxide integration.

To achieve epitaxial $SrRuO_3$ on silicon, various buffer layers that can be epitaxially grown on silicon have been introduced, including yttria-stabilized zirconia (YSZ),[9,26] SrO,[27,28] $SrTiO_3$,[29,30] and $SrTiO_3$ on TiN.[31] Although epitaxy of $SrRuO_3$ on silicon can be realized via these buffer layers, the quality of the $SrRuO_3$ films on silicon still cannot compete with typical $SrRuO_3$ films grown on single-crystal oxide substrates, in terms of both structural perfection [as evaluated by the width of the rocking curve (ω scan) of x-ray diffraction (XRD)] and electrical transport characteristics [as assessed by the residual resistivity ratio ($\mathrm{RRR} = \rho_{300\,\mathrm{K}}/\rho_{4\,\mathrm{K}}$)]. For example, the highest RRR reported for $SrRuO_3$ films on silicon is ~3,[31] indicating significant room for improvement in the transport properties of $SrRuO_3$ on silicon.

Various growth techniques have been utilized for the growth of $SrRuO_3$ on conventional single-crystal oxide substrates. These include 90° off-axis sputtering,[32,33] pulsed-laser deposition (PLD),[10] reactive evaporation,[34–36] molecular-beam epitaxy (MBE),[37,38] metal-organic chemical vapor deposition,[39] and chemical solution deposition.[40] For the integration of epitaxial $SrRuO_3$ with silicon, usually more than one growth technique is involved due to the step for growing the epitaxial buffer layer. For example, in the study of Park *et al.*,[41] the $SrTiO_3$ buffer layer on silicon was grown by MBE while the $SrRuO_3$ film was subsequently deposited by off-axis sputtering. Compared with a combination of multiple growth techniques, which typically involves an air exposure of the buffer layer during the transfer of the sample from one growth chamber to the other (assuming that the two growth chambers are not connected under vacuum), an individual growth method for both the buffer layer and the $SrRuO_3$ film can avoid exposing the buffer layer surface to air and is preferred for the preparation of epitaxial heterostructures. To our knowledge, there is no report of MBE-grown epitaxial $SrRuO_3$ films on silicon although $SrRuO_3$ films of very high quality can be grown on single-crystal oxide substrates by MBE.[38,42]

Here we report the *in situ* integration of $SrRuO_3$ thin films on $SrTiO_3$-buffered (001) Si via MBE. By *in situ*, we mean that the $SrRuO_3$ film was grown on an $SrTiO_3$ film on silicon without removing, etching, or post-annealing the $SrTiO_3$/(001) Si stack outside of vacuum after the $SrTiO_3$ growth on silicon. The resulting films have the highest structural, transport, and magnetic properties among all $SrRuO_3$ films on silicon reported to date;[31,41] these properties are comparable to those of $SrRuO_3$ films grown directly on perovskite single crystals by thin film growth techniques other than MBE.[10,32,33,43–46]

Both the $SrTiO_3$ and $SrRuO_3$ films were grown in a Veeco Gen10 dual-chamber MBE system on 2″ commercial silicon wafers (*p*-type, boron doped, and resistivity >10 Ω cm). The base pressure of the chamber was in the upper 10^{-9} Torr range. Both growth chambers are equipped with *in situ* reflection high-energy electron diffraction (RHEED) systems for monitoring the growth of the $SrTiO_3$ and $SrRuO_3$ layers. Substrate temperature is monitored by using either a thermocouple for temperatures below 500 °C or an optical pyrometer with a measurement wavelength of 980 nm for temperatures above 500 °C. Prior to film growth, the silicon substrate was cleaned *ex situ* in an ultraviolet ozone cleaner for 20 min to remove organic contaminants from the surface of the substrate. Molecular beams of strontium, titanium, and ruthenium were generated from elemental sources using a conventional low-temperature effusion cell, a Ti-Ball$^{\mathrm{TM}}$,[47] and an electron-beam evaporator, respectively.

The $SrTiO_3$ layer was formed in the first growth chamber by the epitaxy-by-periodic-annealing method[48–50] for its first 2 nm (5 unit cells) and then with a high temperature codeposition (strontium, titanium, and oxygen all supplied simultaneously) growth step at a substrate growth temperature of

580 °C to achieve a total $SrTiO_3$ film thickness of 14 nm. The stoichiometry of $SrTiO_3$ was calibrated using shuttered RHEED oscillations, and the growth rate of $SrTiO_3$ was determined by the RHEED oscillations that occurred when an $SrTiO_3$ film was codeposited.[51] For each period of the epitaxy-by-periodic-annealing stage, a 2.5 unit-cell-thick layer of $SrTiO_3$ was first codeposited at 300 °C under an oxygen partial pressure of $\sim 5 \times 10^{-8}$ Torr. Then the substrate temperature was raised to 580 °C in vacuum for the annealing stage to enhance the crystalline quality of the as-grown $SrTiO_3$ film. During the high temperature codeposition step, the oxygen partial pressure was maintained at $\sim(5\text{–}8) \times 10^{-8}$ Torr. The growth of the $SrTiO_3$ layer on silicon is described in detail elsewhere.[50]

The 14 nm thick $SrTiO_3$ layer exhibits a rocking curve with a full width at half maximum (FWHM) of 0.01° for the $SrTiO_3$ 001 peak, indicating that the $SrTiO_3$ buffer layer is of high crystalline quality. This $SrTiO_3$ buffer layer serves as an excellent template for the epitaxial growth of $SrRuO_3$, not only due to the small lattice mismatch [~0.64% lattice mismatch for $(001)_p$ $SrRuO_3$ on (001) $SrTiO_3$, where the subscript p denotes pseudocubic indices], but also due to the high crystalline quality of this 14 nm thick $SrTiO_3$ layer.

RHEED patterns along the [100] and [110] azimuths of the 14 nm thick $SrTiO_3$ film at the end of growth are shown in Figs. 1(a) and 1(b), respectively. The sharp streaks indicate that the $SrTiO_3$ film is epitaxial and smooth. As expected from the codeposition growth of the $SrTiO_3$ buffer

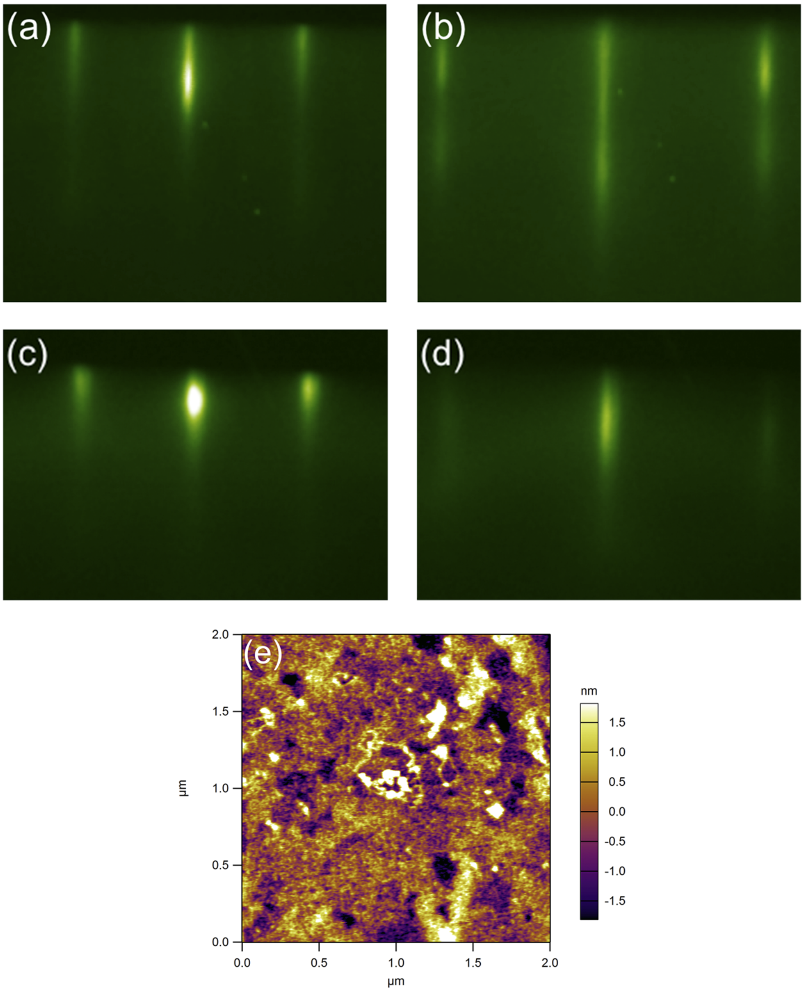

FIG. 1. RHEED patterns of the as-grown 14 nm thick $SrTiO_3$ film viewed along (a) the [100] azimuth and (b) the [110] azimuth of (001) $SrTiO_3$ and RHEED patterns of the as-grown 14 nm thick $SrRuO_3$ film viewed along (c) the $[100]_p$ azimuth and (d) the $[110]_p$ azimuth of $(001)_p$ $SrRuO_3$. (e) Surface morphology of the same sample by AFM.

layer, the surface of the 14 nm thick (001) $SrTiO_3$ layer was found to have mixed termination because half-order streaks are not observed along either the [100] azimuth or [110] azimuth,[49,52] as shown in Figs. 1(a) and 1(b). After the $SrTiO_3$ growth, $SrTiO_3$ on silicon was cooled down in vacuum to a substrate temperature below 200 °C, before being transferred in vacuum into the second growth chamber for the $SrRuO_3$ growth. During this process, no *ex situ* annealing[41] or chemical treatment of the 14 nm thick $SrTiO_3$ film was involved. After heating up to 660-700 °C in the second chamber for the growth of the $SrRuO_3$ film under a 1×10^{-6} Torr mixture of ~10% O_3 + 90% O_2, the surface of the 14 nm thick $SrTiO_3$ became TiO_2-terminated, as is evident from the surface reconstruction that it exhibited shown in Fig. S1 of the supplementary material.[49] Accordingly, we first deposited a submonolayer amount of SrO to neutralize the surface before the growth of the $SrRuO_3$ film.

The $SrRuO_3$ film was grown under adsorption-controlled growth conditions.[42] Unlike the growth of $SrTiO_3$, which needs careful calibration to provide 1:1 matched fluxes of strontium and titanium[51] to yield a stoichiometric $SrTiO_3$ film,[53] the stoichiometry of the $SrRuO_3$ film grown by adsorption-controlled growth is ensured by providing an excess ruthenium flux to the growing film and exploiting thermodynamics to precisely desorb the excess ruthenium in the form RuO_x(g).[42] We grew the $SrRuO_3$ film at a substrate temperature of 660-700 °C (measured using the optical pyrometer) and an oxidant (a mixture of ~10% O_3 + 90% O_2) background pressure of 1×10^{-6} Torr. After growth, the film was cooled down under a chamber background pressure of $\sim 2 \times 10^{-7}$ Torr of the same oxidant (a mixture of ~10% O_3 + 90% O_2) until the substrate temperature reached ~150 °C.

The RHEED patterns of the 14 nm thick $SrRuO_3$ film along the $[100]_p$ and $[110]_p$ azimuths are shown in Figs. 1(c) and 1(d), respectively. These figures show that the $SrRuO_3$ film is also epitaxial and smooth. The surface morphology of the heterostructure was further examined via *ex situ* atomic force microscopy (AFM) using an Asylum Research MFP-3D in tapping mode, as is shown in Fig. 1(e). The rms roughness of the heterostructure is ~8 Å, which is consistent with the streaky RHEED patterns of the $SrRuO_3$ film. A height histogram of the AFM image is shown in Fig. S2 of the supplementary material; it exhibits a Gaussian distribution of step heights.

The epitaxial nature and the crystalline quality of the heterostructure were further assessed *ex situ* by XRD with both Rigaku SmartLab and PANalytical X'Pert four-circle x-ray diffractometers utilizing Cu $K_{\alpha 1}$ radiation. Figure 2(a) shows the XRD θ-2θ scan of the same heterostructure characterized in Fig. 1. The appearance of only 00ℓ reflections indicates that the heterostructure is epitaxial and phase-pure. The intense Bragg peaks reflect the high structural perfection of the perovskite $SrTiO_3$ buffer layer and the $SrRuO_3$ film. The thickness fringes indicate that the interfaces of the heterostructure are smooth. Using a Nelson-Riley fit, the out-of-plane lattice parameter of the $SrRuO_3$ film is found to be 3.935 ± 0.005 Å, which manifests that the $SrRuO_3$ film is relaxed on the 14 nm thick $SrTiO_3$ film on silicon. This might originate from the large thermal expansion difference between $SrRuO_3$ (averaging 1.03×10^{-5} K^{-1} between 150 °C and 800 °C)[54] and silicon (averaging 3.7×10^{-6} K^{-1} between room temperature and 720 °C).[55] Even though a commensurate film of $(001)_p$ $SrRuO_3$ is compressively strained to (001) $SrTiO_3$, the tensile strain induced by the thermal expansion difference to the underlying silicon substrate during the cool-down process can make the lattice parameter of the $SrRuO_3$ film relax to its bulk value.

The rocking curves of both the $SrTiO_3$ 001 and the $SrRuO_3$ 001_p peaks were measured, together with that of the Si 004 peak. Figure 2(b) shows that the FWHM of the $SrTiO_3$ 001 peak is 0.01°; this FWHM is comparable to single crystal $SrTiO_3$ substrates.[56] With a FWHM of the $SrRuO_3$ 001_p peak of 0.01°, the 14 nm thick $SrRuO_3$ film on $SrTiO_3$ on silicon has the narrowest rocking curve ever reported for $SrRuO_3$ films on silicon;[28,41] this FWHM is comparable to most $SrRuO_3$ films grown on single-crystal oxide substrates.[34,38,43,44] Representative rocking curve FWHM values of $SrRuO_3$ films reported in the literature are summarized in comparison with our result for $SrRuO_3$ on silicon in Fig. S3(a) of the supplementary material. The in-plane orientation relationship between the film and the silicon substrate was confirmed with a ϕ scan: (001) $SrTiO_3$ ∥ $(001)_p$ $SrRuO_3$ ∥ (001) Si and [100] $SrTiO_3$ ∥ $[100]_p$ $SrRuO_3$ ∥ [110] Si, as is shown in Fig. 2(c).

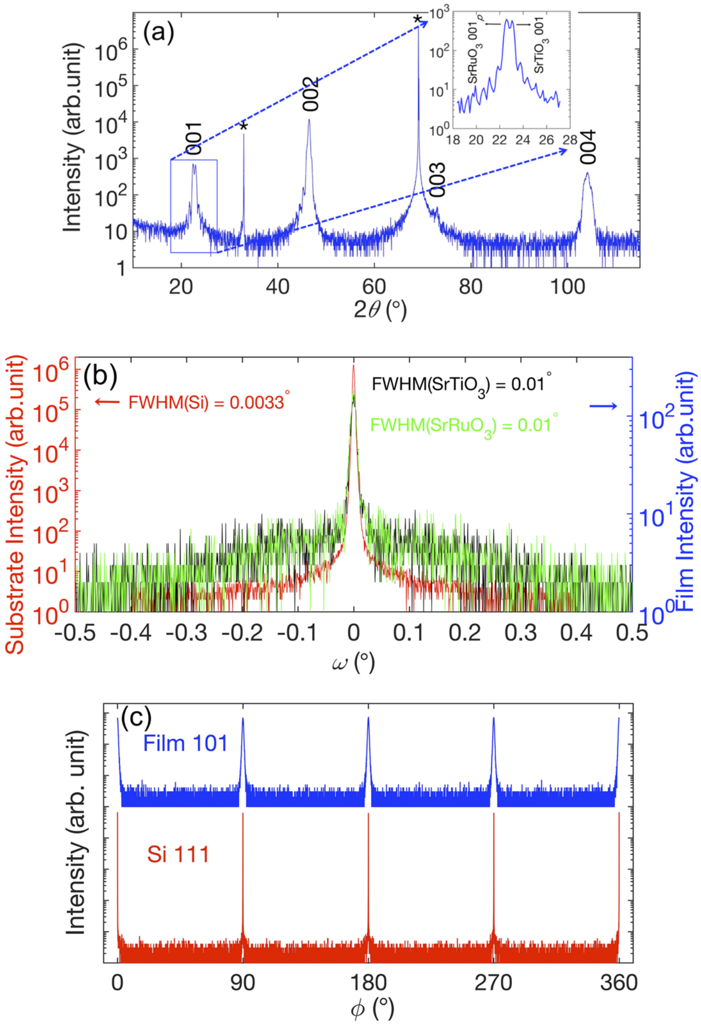

FIG. 2. (a) XRD θ-2θ scan of the 14 nm thick SrRuO$_3$ film on 14 nm thick SrTiO$_3$ film on silicon. Peaks from the silicon substrate are indicated with an asterisk. Thickness fringes manifest that the interfaces of the heterostructure are smooth. The inset shows an enlarged view of the 001$_p$ film peak. (b) Rocking curves of the SrTiO$_3$ 001 and the SrRuO$_3$ 001$_p$ peaks of the same heterostructure. These peaks both have FWHMs of 0.01°. The rocking curve of the Si 004 peak is overlaid with those of the films. (c) ϕ scans of the same sample indicate that the in-plane epitaxial relationship is cube-on-cube with the $[100]_p$ direction of the perovskite film aligned with the [110] direction of the Si (001) surface. The FWHM of the film ϕ scan is 0.92°. The ϕ scans are offset from each other along the vertical axis for clarity.

The resistivity (ρ) vs. temperature (T) of the same sample was measured in a standard four-probe van der Pauw geometry with wire-bonded contacts made using aluminum wire in a Quantum Design physical property measurement system (PPMS). The result is shown in Fig. 3(a). The RRR is ∼11, which is the largest RRR reported for SrRuO$_3$ films on silicon;[31,57] it is comparable to the RRR values of SrRuO$_3$ films grown on single-crystal oxide substrates by PLD[43–45] but is inferior to those of SrRuO$_3$ films grown on single-crystal oxide substrates by MBE.[42] A general comparison of the RRRs of SrRuO$_3$ films in the literature is summarized in Fig. S3(b) of the supplementary material.

The linear relationship between resistivity and T^2 for temperatures below 10 K [Fig. 3(c)] is consistent with the Fermi liquid behavior observed in SrRuO$_3$ films grown on single-crystal SrTiO$_3$ substrates by reactive evaporation.[21] There is a clear kink observed at ∼160 K in Fig. 3(a), indicating the change in the scattering rate due to the paramagnetic-to-ferromagnetic transition. The paramagnetic-to-ferromagnetic transition temperature is approximately given by the temperature at

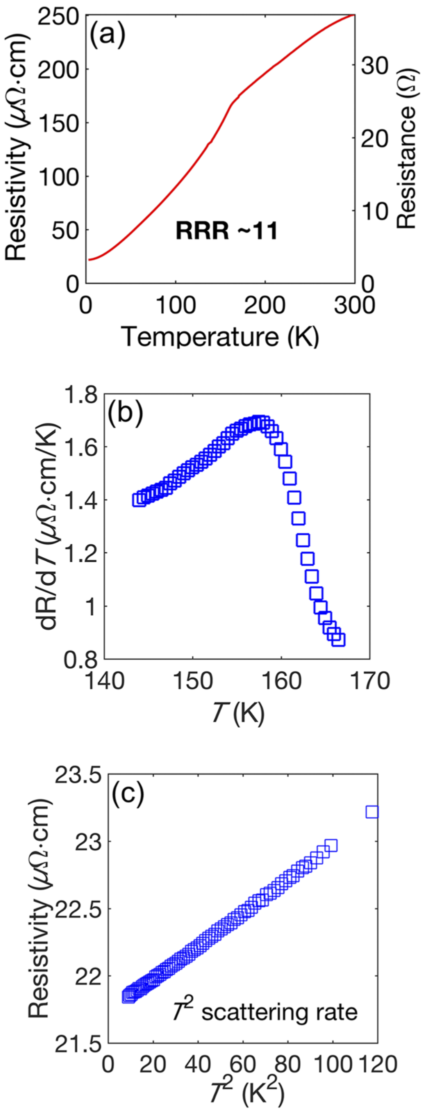

FIG. 3. Transport properties of the 14 nm thick $SrRuO_3$ film of the same sample. (a) The $SrRuO_3$ film exhibits a resistivity of ~250 $\mu\Omega$ cm at room temperature and metallic behavior at low temperature. (b) The derivative of the resistivity as a function of T indicates that the paramagnetic-to-ferromagnetic transition temperature is at ~160 K. (c) In the low-temperature regime, resistivity scales linearly with T^2, indicating the Fermi liquid behavior at low temperature for the $SrRuO_3$ film.

which the derivative of the temperature-dependent resistivity is maximal, as is shown in Fig. 3(b). The transition temperature of ~160 K is close to that of bulk $SrRuO_3$ single crystals,[58] which indicates that the 14 nm thick $SrRuO_3$ film is relaxed on the $SrTiO_3$-buffered silicon. A comparison of the Curie temperatures of $SrRuO_3$ films in the literature is summarized in Fig. S3(c) of the supplementary material.

The magnetic properties of the same sample were measured with a superconducting quantum interference device (SQUID) from Quantum Design. The sample was cooled under a 0.1 T field, and the in-plane (along $[100]_p$) and out-of-plane magnetization was measured as a function of temperature. The result is shown in Fig. 4(a). The in-plane and out-of-plane magnetic hysteresis loops measured at 10 K are shown in Fig. 4(b). Both loops show similar hysteresis with a large squareness (a ratio between the remanent and saturation magnetization) implying strong magnetocrystalline anisotropy of the $SrRuO_3$ film. The in-plane and out-of-plane saturation magnetization at 10 K is ~0.75 μ_B and ~0.61 μ_B per ruthenium atom, respectively. These values are again comparable to the results from

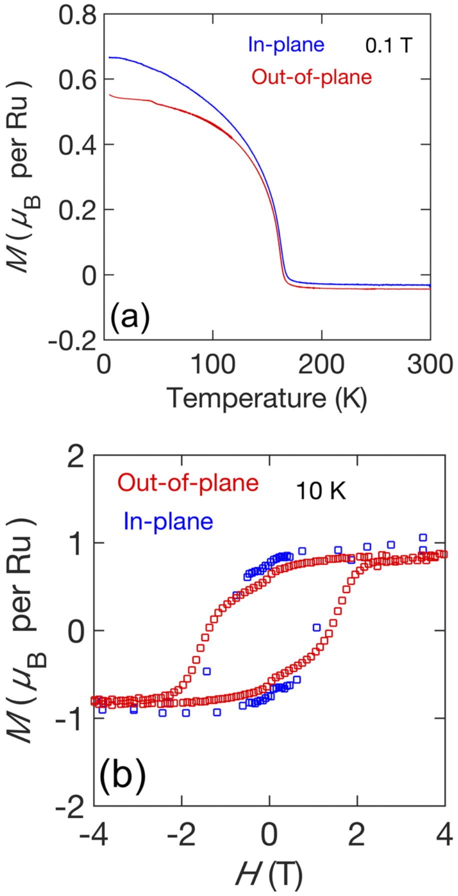

FIG. 4. (a) The in-plane and out-of-plane magnetization as a function of temperature measured on the same sample cooled under 0.1 T. (b) In-plane and out-of-plane magnetic hysteresis loops measured at 10 K. For the in-plane measurement, H is along the $[100]_p$ of $SrRuO_3$, and for the out-of-plane measurement, H is along the $[001]_p$ of $SrRuO_3$.

$SrRuO_3$ films grown directly on $SrTiO_3$ single crystals[59,60] and are among the highest for $SrRuO_3$ films on silicon.[31]

The $SrRuO_3$/$SrTiO_3$ and $SrTiO_3$/Si interfaces in the same sample were examined by high angle annular dark field (HAADF) scanning transmission electron microscopy (STEM) using a Titan microscope operated at 300 keV. As is shown in Fig. 5(a), the interface between the 14 nm thick $SrRuO_3$ layer and the 14 nm thick $SrTiO_3$ layer is abrupt on the atomic scale. White, cyan, and green circles indicate strontium, ruthenium, and titanium atoms, respectively. Figures S4(a) and S4(b) of the supplementary material show the microstructure and thickness uniformity of the same sample at lower magnification. These HAADF-STEM images indicate that the $SrTiO_3$ buffer layer and the $SrRuO_3$ film both exhibit a high degree of crystalline perfection and that the sample is uniform over a large scale. There is an amorphous SiO_2 layer between the $SrTiO_3$ film and the silicon substrate, which originates from the diffusion of oxygen through the $SrTiO_3$ layer during the growth of either the $SrTiO_3$ or the $SrRuO_3$ film. This amorphous layer is typical for epitaxial $SrTiO_3$ films grown on silicon and is seen in other related studies.[61–64]

Note that despite the high crystalline perfection and electrical characteristics, opportunities remain to further improve the quality of $SrRuO_3$ films on $SrTiO_3$-buffered silicon. For example, the FWHM of the ϕ scan is relatively large, indicating a considerable amount of in-plane mosaic spread of the $SrRuO_3$ film. Also, $SrRuO_3$ samples with less surface roughness are needed for applications where interfaces are critical. Finally, the temperatures used for the deposition of high quality $SrRuO_3$ films (in our study as well as in the work by others on single-crystal perovskite substrates)

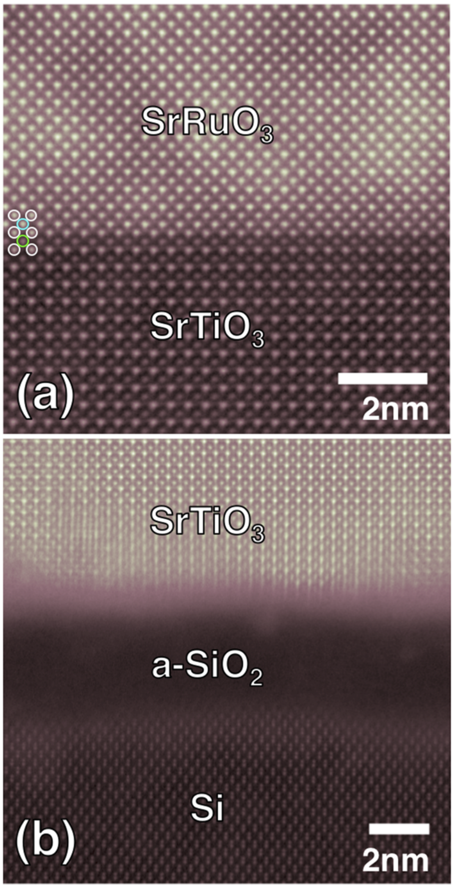

FIG. 5. HAADF-STEM images of the same sample characterized in Figs. 1–4. The interface between the $SrRuO_3$ layer and the $SrTiO_3$ layer is shown in (a). An amorphous SiO_2 layer is evident between the $SrTiO_3$ film and the silicon substrate in (b). This is due to the oxygen diffusion through the $SrTiO_3$ film during the film growth.

are too high to be compatible with underlying complementary metal-oxide-semiconductor (CMOS) circuitry.

In summary, we have integrated $SrRuO_3$ films on $SrTiO_3$-buffered silicon with a film quality similar to $SrRuO_3$ films grown on single-crystal oxide substrates via thin film growth techniques other than MBE. This integration paves the way toward integrating multi-functional devices of record-performance on the workhorse of semiconductor technology, silicon.

See supplementary material for additional details on the surface termination of the $SrTiO_3$ buffer layer, AFM height histogram, comparison of rocking curve FWHM, RRR, and Curie temperature of our sample with those of representative results from the literature, and additional STEM images of the sample.

Z.W., H.P.N., A.S.H., and D.G.S. gratefully acknowledge the support from a GRO “functional oxides” project from the Samsung Advanced Institute of Technology and support from the W.M. Keck Foundation. G.C.C. and D.A.M. acknowledge support by the National Science Foundation [Platform for the Accelerated Realization, Analysis, and Discovery of Interface Materials (PARADIM)] under Cooperative Agreement No. DMR-1539918. G.C.C. acknowledges support from the Alfred P. Sloan Foundation and the DOE CSGF (No. DE-FG02-97ER25308). This work made use of the Cornell Center for Materials Research (CCMR) Shared Facilities, which are supported through the NSF MRSEC program (No. DMR-1719875). Substrate preparation was performed in part at the Cornell NanoScale Facility, a member of the National Nanotechnology Coordinated Infrastructure (NNCI), which is supported by the NSF (Grant No. ECCS-15420819).

[1] G. Koster, L. Klein, W. Siemons, G. Rijnders, J. S. Dodge, C. B. Eom, D. H. A. Blank, and M. R. Beasley, Rev. Mod. Phys. **84**, 253 (2012).
[2] W. Bensch, H. W. Schmalle, and A. Reller, Solid State Ionics **43**, 171 (1990).
[3] H. N. Lee, H. M. Christen, M. F. Chisholm, C. M. Rouleau, and D. H. Lowndes, Appl. Phys. Lett. **84**, 4107 (2004).
[4] F. Kubel and H. Schmid, Acta Crystallogr., Sect. B: Struct. Sci. **46**, 698 (1990).
[5] R. H. Buttner and E. N. Maslen, Acta Crystallogr., Sect. B: Struct. Sci. **48**, 764 (1992).
[6] T. Siegrist, S. Sunshine, D. W. Murphy, R. J. Cava, and S. M. Zahurak, Phys. Rev. B **35**, 7137 (1987).
[7] R. J. Nelmes and W. F. Kuhs, Solid State Commun. **54**, 721 (1985).
[8] S. Teslic and T. Egami, Acta Crystallogr., Sect. B: Struct. Sci. **54**, 750 (1998).
[9] C. B. Eom, R. B. Van Dover, J. M. Phillips, D. J. Werder, J. H. Marshall, C. H. Chen, R. J. Cava, R. M. Fleming, and D. K. Fork, Appl. Phys. Lett. **63**, 2570 (1993).
[10] X. D. Wu, S. R. Foltyn, R. C. Dye, Y. Coulter, and R. E. Muenchausen, Appl. Phys. Lett. **62**, 2434 (1993).
[11] L. Antognazza, K. Char, T. H. Geballe, L. L. H. King, and A. W. Sleight, Appl. Phys. Lett. **63**, 1005 (1993).
[12] L. Klein, J. S. Dodge, T. H. Geballe, A. Kapitulnik, A. F. Marshall, L. Antognazza, and K. Char, Appl. Phys. Lett. **66**, 2427 (1995).
[13] T. Fujii, M. Kawasaki, A. Sawa, H. Akoh, Y. Kawazoe, and Y. Tokura, Appl. Phys. Lett. **86**, 012107 (2005).
[14] J. Rodríguez Contreras, H. Kohlstedt, U. Poppe, R. Waser, C. Buchal, and N. A. Pertsev, Appl. Phys. Lett. **83**, 4595 (2003).
[15] S. Thota, Q. Zhang, F. Guillou, U. Lüders, N. Barrier, W. Prellier, A. Wahl, and P. Padhan, Appl. Phys. Lett. **97**, 112506 (2010).
[16] C. H. Ahn, T. Tybell, L. Antognazza, K. Char, R. H. Hammond, M. R. Beasley, Ø. Fischer, and J.-M. Triscone, Science **276**, 1100 (1997).
[17] X. Martí, F. Sánchez, J. Fontcuberta, M. V. García-Cuenca, C. Ferrater, and M. Varela, J. Appl. Phys. **99**, 08P302 (2006).
[18] J. M. Rondinelli, M. Stengel, and N. A. Spaldin, Nat. Nanotechnol. **3**, 46 (2007).
[19] S. Y. Yang, L. W. Martin, S. J. Byrnes, T. E. Conry, S. R. Basu, D. Paran, L. Reichertz, J. Ihlefeld, C. Adamo, A. Melville, Y.-H. Chu, C.-H. Yang, J. L. Musfeldt, D. G. Schlom, J. W. Ager, and R. Ramesh, Appl. Phys. Lett. **95**, 062909 (2009).
[20] H. J. Liu, J. C. Wang, D. Y. Cho, K. T. Ho, J. C. Lin, B. C. Huang, Y. W. Fang, Y. M. Zhu, Q. Zhan, L. Xie, X. Q. Pan, Y. P. Chiu, C. G. Duan, J. H. He, and Y. H. Chu, "Giant photoresponse in quantized $SrRuO_3$ monolayer at oxide interfaces," ACS Photonics **5**, 1041 (2018).
[21] A. P. Mackenzie, J. W. Reiner, A. W. Tyler, L. M. Galvin, S. R. Julian, M. R. Beasley, T. H. Geballe, and A. Kapitulnik, Phys. Rev. B **58**, R13318 (1998).
[22] L. Klein, J. S. Dodge, C. H. Ahn, G. J. Snyder, T. H. Geballe, M. R. Beasley, and A. Kapitulnik, Phys. Rev. Lett. **77**, 2774 (1996).
[23] J. Matsuno, N. Ogawa, K. Yasuda, F. Kagawa, W. Koshibae, N. Nagaosa, Y. Tokura, and M. Kawasaki, Sci. Adv. **2**, e1600304 (2016).
[24] M. Wahler, N. Homonnay, T. Richter, A. Müller, C. Eisenschmidt, B. Fuhrmann, and G. Schmidt, Sci. Rep. **6**, 28727 (2016).
[25] K. Watanabe, M. Ami, and M. Tanaka, Mater. Res. Bull. **32**, 83 (1997).
[26] S. Y. Hou, J. Kwo, R. K. Watts, J.-Y. Cheng, and D. K. Fork, Appl. Phys. Lett. **67**, 1387 (1995).
[27] T. Higuchi, Y. Chen, J. Koike, S. Iwashita, M. Ishida, and T. Shimoda, Jpn. J. Appl. Phys., Part I **41**, 6867 (2002).
[28] T. Higuchi, Y. Chen, J. Koike, S. Iwashita, M. Ishida, and T. Shimoda, Jpn. J. Appl. Phys., Part II **41**, L481 (2002).
[29] J. Wang, H. Zheng, Z. Ma, S. Prasertchoung, M. Wuttig, R. Droopad, J. Yu, K. Eisenbeiser, and R. Ramesh, Appl. Phys. Lett. **85**, 2574 (2004).
[30] L. W. Martin, Y. H. Chu, Q. Zhan, R. Ramesh, S. J. Han, S. X. Wang, M. Warusawithana, and D. G. Schlom, Appl. Phys. Lett. **91**, 172513 (2007).
[31] M. Zheng and W. Wang, ACS Appl. Mater. Interfaces **8**, 14012 (2016).
[32] C. B. Eom, R. J. Cava, R. M. Fleming, J. M. Phillips, R. B. vanDover, J. H. Marshall, J. W. P. Hsu, J. J. Krajewski, and W. F. Peck, Science **258**, 1766 (1992).
[33] Q. Gan, R. A. Rao, C. B. Eom, J. L. Garrett, and M. Lee, Appl. Phys. Lett. **72**, 978 (1998).
[34] L. Klein, J. S. Dodge, C. H. Ahn, J. W. Reiner, L. Mieville, T. H. Geballe, M. R. Beasley, and A. Kapitulnik, J. Phys.: Condens. Matter **8**, 10111 (1996).
[35] M. Izumi, K. Nakazawa, Y. Bando, Y. Yoneda, and H. Terauchi, J. Phys. Soc. Jpn. **66**, 3893 (1997).
[36] L. Klein, Y. Kats, A. F. Marshall, J. W. Reiner, T. H. Geballe, M. R. Beasley, and A. Kapitulnik, Phys. Rev. Lett. **84**, 6090 (2000).
[37] W. Tian, J. H. Haeni, D. G. Schlom, E. Hutchinson, B. L. Sheu, M. M. Rosario, P. Schiffer, Y. Liu, M. A. Zurbuchen, and X. Q. Pan, Appl. Phys. Lett. **90**, 022507 (2007).
[38] D. E. Shai, C. Adamo, D. W. Shen, C. M. Brooks, J. W. Harter, E. J. Monkman, B. Burganov, D. G. Schlom, and K. M. Shen, Phys. Rev. Lett. **110**, 087004 (2013).
[39] N. Okuda, K. Saito, and H. Funakubo, Jpn. J. Appl. Phys., Part I **39**, 572 (2000).
[40] D. Yang, X. Tang, R. Wei, Z. Hui, W. Song, X. Zhu, and Y. Sun, J. Alloys Compd. **682**, 154 (2016).
[41] J. W. Park, S. H. Baek, C. W. Bark, M. D. Biegalski, and C. B. Eom, Appl. Phys. Lett. **95**, 061902 (2009).
[42] H. P. Nair, Y. Liu, J. P. Ruf, N. J. Schreiber, S. Shang, D. J. Baek, B. H. Goodge, L. F. Kourkoutis, Z. Liu, K. M. Shen, and D. G. Schlom, APL Mater. **6**, 046101 (2018).
[43] O. Tsuyoshi and T. Kazunori, Appl. Phys. Express **4**, 025501 (2011).
[44] D. Kan, R. Aso, H. Kurata, and Y. Shimakawa, J. Appl. Phys. **113**, 173912 (2013).
[45] J. Thompson, J. Nichols, S. Lee, S. Ryee, J. H. Gruenewald, J. G. Connell, M. Souri, J. M. Johnson, J. Hwang, M. J. Han, H. N. Lee, D.-W. Kim, and S. S. A. Seo, Appl. Phys. Lett. **109**, 161902 (2016).
[46] F. Chu, Q. X. Jia, G. Landrum, X. D. Wu, M. Hawley, and T. E. Mitchell, J. Electron. Mater. **25**, 1754 (1996).
[47] C. D. Theis and D. G. Schlom, J. Vac. Sci. Technol., A **14**, 2677 (1996).

[48] H. Li, X. Hu, Y. Wei, Z. Yu, X. Zhang, R. Droopad, A. A. Demkov, J. Edwards, K. Moore, W. Ooms, J. Kulik, and P. Fejes, J. Appl. Phys. **93**, 4521 (2003).

[49] M. P. Warusawithana, C. Cen, C. R. Sleasman, J. C. Woicik, Y. Li, L. F. Kourkoutis, J. A. Klug, H. Li, P. Ryan, L. P. Wang, M. Bedzyk, D. A. Muller, L. Q. Chen, J. Levy, and D. G. Schlom, Science **324**, 367 (2009).

[50] Z. Wang, D. Baek, B. Goodge, M. Zachman, X. Huang, X. Bai, C. M. Brooks, H. Paik, A. B. Mei, J. D. Brock, J. P. Maria, L. F. Kourkoutis, and D. G. Schlom (unpublished).

[51] J. H. Haeni, C. D. Theis, and D. G. Schlom, J. Electroceram. **4**, 385 (2000).

[52] K. Iijima, T. Terashima, Y. Bando, K. Kamigaki, and H. Terauchi, J. Appl. Phys. **72**, 2840 (1992).

[53] C. M. Brooks, L. F. Kourkoutis, T. Heeg, J. Schubert, D. A. Muller, and D. G. Schlom, Appl. Phys. Lett. **94**, 162905 (2009).

[54] S. Yamanaka, T. Maekawa, H. Muta, T. Matsuda, S. Kobayashi, and K. Kurosaki, J. Solid State Chem. **177**, 3484 (2004).

[55] Y. S. Touloukian, R. K. Kirby, R. E. Taylor, and T. Y. R. Lee, "Thermophysical properties of matter," in *Thermal Expansion-Nonmetallic Solids*, The TPRC Data Series (Plenum, NY, 1977), Vol. 13.

[56] D. G. Schlom, L. Q. Chen, X. Q. Pan, A. Schmehl, and M. A. Zurbuchen, J. Am. Ceram. Soc. **91**, 2429 (2008).

[57] M. Zhu, X. Dong, Y. Chen, F. Xue, J. Lian, L. Xiao, G. Ding, and G. Wang, Ceram. Int. **42**, 13925 (2016).

[58] G. Cao, S. McCall, M. Shepard, J. E. Crow, and R. P. Guertin, Phys. Rev. B **56**, 321 (1997).

[59] M. Zheng, X. Li, W. Xiao, W. Wang, and H. Ni, Appl. Phys. Lett. **111**, 152405 (2017).

[60] S. Woo, S. A. Lee, H. Mun, Y. G. Choi, C. J. Zhung, S. Shin, M. Lacotte, A. David, W. Prellier, T. Park, W. N. Kang, J. S. Lee, S. W. Kim, and W. S. Choi, Nanoscale **10**, 4377 (2018).

[61] D. B. Fenner, A. M. Viano, D. K. Fork, G. A. N. Connell, J. B. Boyce, F. A. Ponce, and J. C. Tramontana, J. Appl. Phys. **69**, 2176 (1991).

[62] Y. Chen, J. Koike, T. Higuchi, S. Iwashita, M. Ishida, and T. Shimoda, Jpn. J. Appl. Phys., Part II **40**, L1305 (2001).

[63] S. Abel, T. Stöferle, C. Marchiori, C. Rossel, M. D. Rossell, R. Erni, D. Caimi, M. Sousa, A. Chelnokov, B. J. Offrein, and J. Fompeyrine, Nat. Commun. **4**, 1671 (2013).

[64] R. Guo, Z. Wang, S. Zeng, K. Han, L. Huang, D. G. Schlom, T. Venkatesan, Ariando, and J. Chen, Sci. Rep. **5**, 12576 (2015).

Supplementary Material for

Epitaxial integration and properties of $SrRuO_3$ on silicon

Zhe Wang*,[1] Hari P. Nair*,[2] Gabriela C. Correa,[2] Jaewoo Jeong,[3]
Kiyoung Lee,[4] Eun Sun Kim,[5] Ariel Seidner H.,[2] Chang Seung Lee,[4]
Han Jin Lim,[5] David A. Muller,[1,6] and Darrell G. Schlom,[2,6,a)]

[1]*School of Applied and Engineering Physics, Cornell University, Ithaca, NY, 14853, USA*

[2]*Department of Materials Science and Engineering, Cornell University, Ithaca, NY, 14853, USA*

[3]*New Memory Technology Lab, Semiconductor R&D Center, Samsung Electronics, Milpitas, California 95053, USA*

[4]*Platform Technology Laboratory, Samsung Advanced Institute of Technology (SAIT), Samsung Electronics, 130 Samsung-ro, Yeongtong-gu, Suwon-si, Gyeonggi-do, 16678, Korea*

[5]*Samsung Semiconductor R&D Center 1, Samsungjeonja-ro, Hwaseong-si, Gyeonggi-do, 18448, Korea*

[6]*Kavli Institute at Cornell for Nanoscale Science, Ithaca, NY, 14853, USA*

---

a) Author to whom correspondence should be addressed. Electronic mail: schlom@cornell.edu.

* These authors contributed equally to this work.

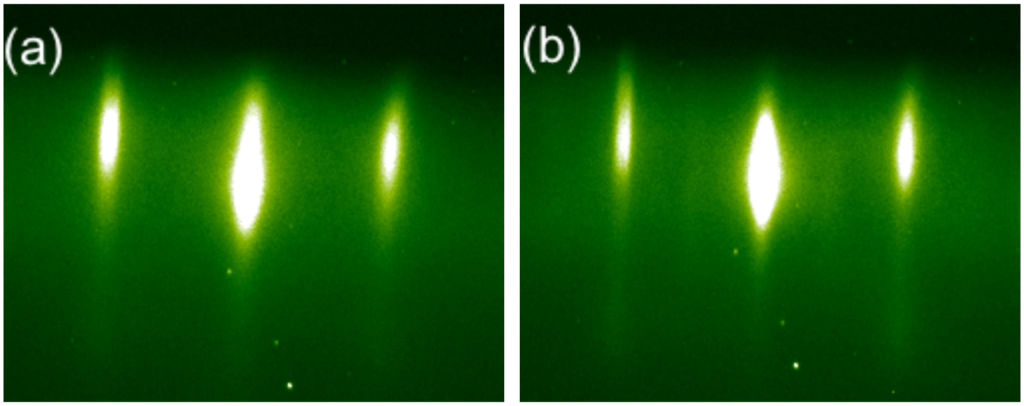

FIG. S1 RHEED patterns of a 15 nm thick $SrTiO_3$ on silicon viewed along the [100] azimuth of $SrTiO_3$. (a) The as grown 15 nm thick $SrTiO_3$ on silicon. (b) After heating up to 660-700 °C under 1×10^{-6} Torr ~10% O_3 + 90% O_2. The half order streaks observed in (b) indicate that the surface was TiO_2 dominated. Correspondingly, we deposited a suitable amount of SrO to neutralize the surface before the growth of the $SrRuO_3$ film.

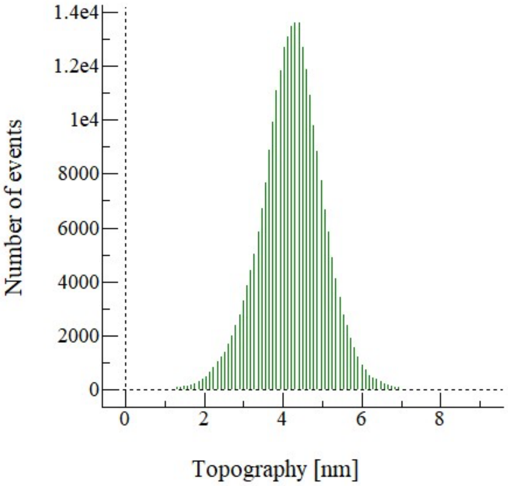

FIG. S2 A height histogram of the AFM image of the14 nm thick $SrRuO_3$ on 14 nm thick $SrTiO_3$ on silicon sample.

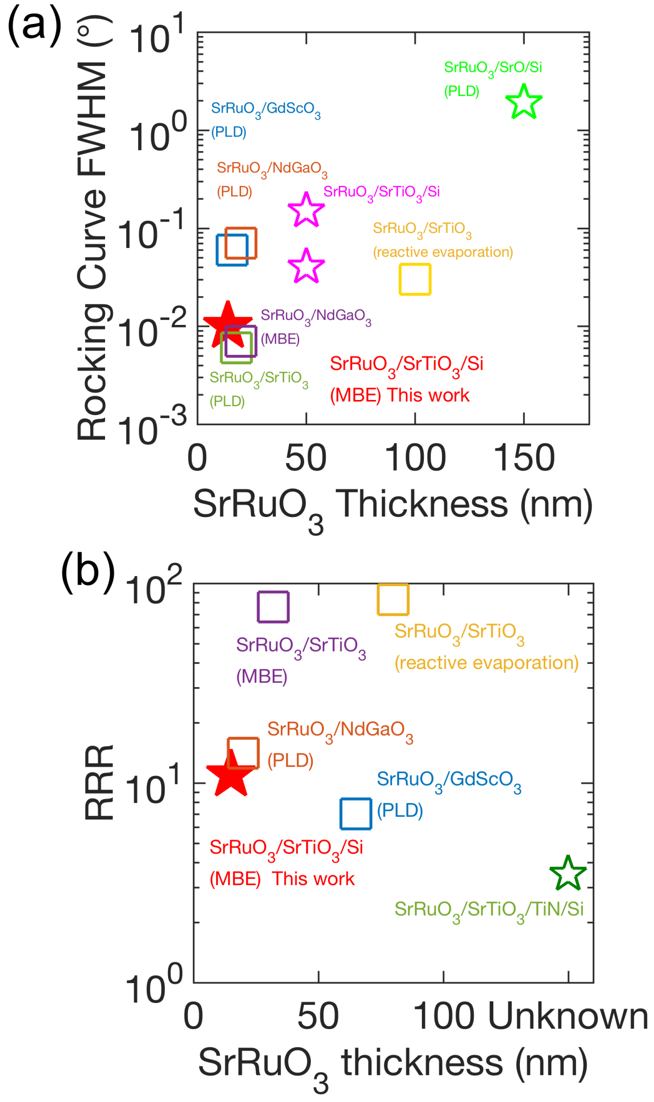
(a)
Rocking Curve FWHM (°)
10^1
10^0
10^{-1}
10^{-2}
10^{-3}
0
50
100
150
$SrRuO_3$ Thickness (nm)
$SrRuO_3/SrO/Si$
(PLD)
$SrRuO_3/GdScO_3$
(PLD)
$SrRuO_3/NdGaO_3$
(PLD)
$SrRuO_3/SrTiO_3/Si$
$SrRuO_3/SrTiO_3$
(reactive evaporation)
$SrRuO_3/NdGaO_3$
(MBE)
$SrRuO_3/SrTiO_3/Si$
(MBE) This work
$SrRuO_3/SrTiO_3$
(PLD)
(b)
RRR
10^2
10^1
10^0
0
50
100 Unknown
$SrRuO_3$ thickness (nm)
$SrRuO_3/SrTiO_3$
(MBE)
$SrRuO_3/SrTiO_3$
(reactive evaporation)
$SrRuO_3/NdGaO_3$
(PLD)
$SrRuO_3/GdScO_3$
(PLD)
$SrRuO_3/SrTiO_3/Si$
(MBE) This work
$SrRuO_3/SrTiO_3/TiN/Si$

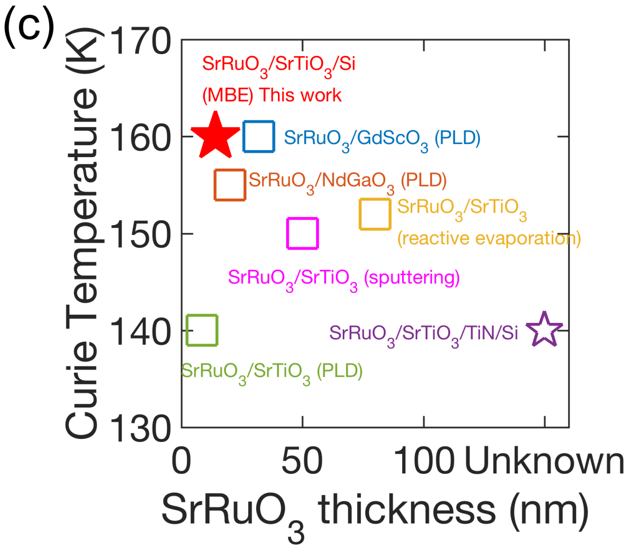

FIG. S3 (a) The Rocking curve FWHM comparison with representative values from the literature. Square-shape data points represent $SrRuO_3$ films grown on single-crystal oxide substrates, and star-shape data points represent $SrRuO_3$ films grown on silicon. The $SrRuO_3/NdGaO_3$ (MBE) data point is from Ref. 38; the $SrRuO_3/SrTiO_3$ (reactive evaporation) data point is from Ref. 34; the $SrRuO_3/NdGaO_3$ (PLD) data point is from Ref. 44; the $SrRuO_3/GdScO_3$ (PLD) data point is from Ref. 45; the $SrRuO_3/SrTiO_3$ (PLD) data point is from Ref. 43; the $SrRuO_3/SrTiO_3/Si$ data points of purple color are from Ref. 41, the two data points represent two $SrRuO_3$ films on $SrTiO_3$ on silicon – the top data point for $SrRuO_3$ on $SrTiO_3$ on silicon without *ex-situ* annealing of the $SrTiO_3$ film on silicon and the bottom data point for $SrRuO_3$ on *ex-situ* annealed $SrTiO_3$ on silicon; the $SrRuO_3/SrO/Si$ (PLD) data point is from Ref. 28. (b) A comparison of the RRR reported for $SrRuO_3$ films grown directly on single-crystal oxide substrates and that of this work, where the $SrRuO_3$ is grown on $SrTiO_3$-buffered silicon. The RRR of our $SrRuO_3$ film on silicon rivals $SrRuO_3$ films grown on single-crystal oxide substrates by PLD, but is inferior to films grown via MBE or reactive evaporation. The $SrRuO_3/SrTiO_3$ (MBE) data point is from Ref. 42; the $SrRuO_3/SrTiO_3$ (reactive evaporation) data point is from Ref. 35; the $SrRuO_3/NdGaO_3$ (PLD) data point is from Ref. 44; the $SrRuO_3/GdScO_3$ (PLD) data point is from Ref. 45; and the $SrRuO_3/SrTiO_3/TiN/Si$ data point is from Ref. 31, the thickness of the sample is unknown. (c) A comparison of the Curie temperature reported for $SrRuO_3$ films grown directly on single-crystal oxide substrates and on $SrTiO_3/TiN$-buffered silicon and that of this work, where the $SrRuO_3$ is grown on $SrTiO_3$-buffered silicon. The $SrRuO_3/GdScO_3$ (PLD) data point is from Ref. 45; the $SrRuO_3/NdGaO_3$ (PLD) data point is from Ref. 44; the $SrRuO_3/SrTiO_3$ (reactive evaporation) data point is from Ref. 35; the $SrRuO_3/SrTiO_3$ (sputtering) data point is from Ref. 32; the $SrRuO_3/SrTiO_3$ (PLD) data point is from Ref. 65; and the $SrRuO_3/SrTiO_3/TiN/Si$ data point is from Ref. 31, the thickness of the sample is unknown. In all three figures, red stars represent this work.

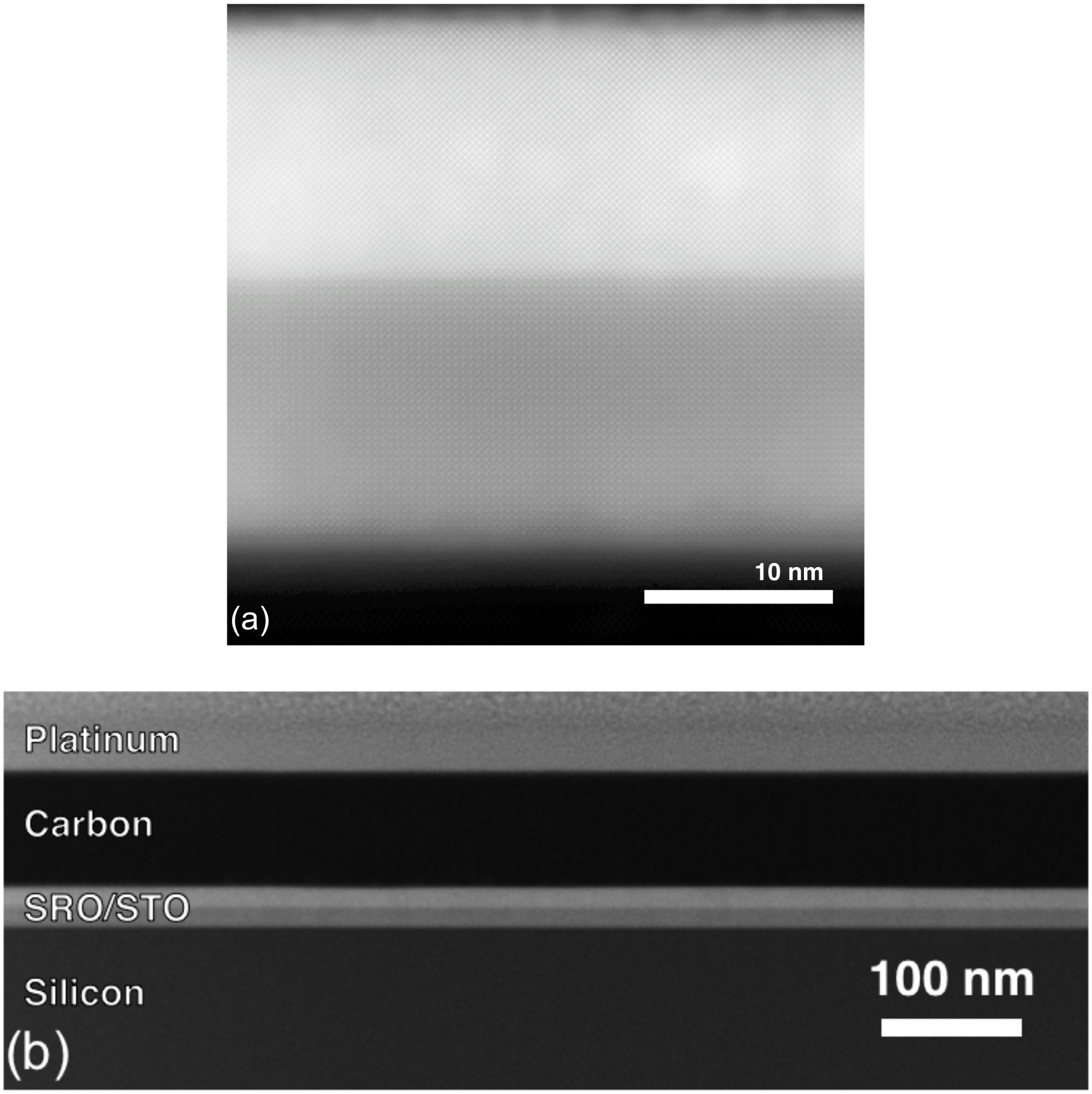

FIG. S4 (a) HAADF-STEM image of the same sample at a lower magnification than Fig. 5. (b) Another HAADF-STEM image at an even lower magnification showing the overall uniformity of the same heterostructure. These images reveal that the interface between the $SrTiO_3$ buffer layer and the $SrRuO_3$ film is atomically abrupt. Further, the $SrTiO_3$ buffer layer and the $SrRuO_3$ film both have high structural perfection.

65 J. Xia, W. Siemons, G. Koster, M. R. Beasley, and A. Kapitulnik, Phys. Rev. B. **79**, 140407 (2009).